NANO LETTERS

pubs.acs.org/NanoLett Letter

Can Light Alter the Yield of Plasmon-Driven Reactions on Gold and Gold–Palladium Nanoplates?

Zhandong Li and Dmitry Kurouski*

Cite This: *Nano Lett.* 2022, 22, 7484–7491 Read Online

ACCESS | Metrics & More | Article Recommendations | SI Supporting Information

ABSTRACT: Noble-metal nanostructures, as well as their bimetallic analogues, catalyze a broad spectrum of plasmon-driven reactions. Catalytic properties of such nanostructures arise from light-generated surface plasmon resonances that decay forming transient hot electrons and holes. Hot carriers with "slower" dissipation rates accumulate on nanostructures generating an electrostatic potential. In this study, we examine whether light intensity can alter the electrostatic potential of mono- and bimetallic nanostructures changing yields of plasmon-driven reactions. Using tip-enhanced Raman spectroscopy (TERS), we quantified the yield of plasmon-driven transformations of 4-nitrobenzenethiol (4-NBT) and 3-mercaptobenzoic acid (3-MBA) on gold and gold–palladium nanoplates (AuNPs and Au@PdNPs, respectively). We found that on AuNPs 3-MBA decarboxylated forming thiophenol (TP), whereas 4-NBT was reduced to DMAB. The yield of both TP and DMAB gradually increased with increasing light intensity. On Au@PdNPs, 3-MBA could be reduced to 3-mercaptophenylmethanol (3-MPM), the yield of which was also directly dependent on the light intensity.

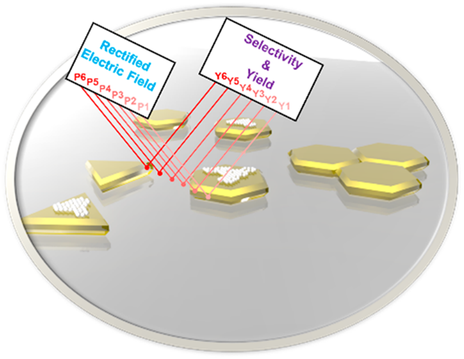

KEYWORDS: *plasmons, TERS, gold–palladium nanoplates, 4-nitrobenzenethiol, 3-mercaptobenzoic acid, thiophenol*

Illumination of noble-metal nanostructures by electromagnetic radiation generates collective oscillations of conductive elections on their surfaces, also known as surface plasmon resonances (SPRs).[1−6] SPRs can dissipate though elastic scattering of photons producing heat.[7,8] Alternatively, SPRs can decay through phase shifting—a nonradiative pathway that is known as Landau damping.[9−12] Phase shifting yields both negatively charged hot electrons and positively charged holes.[7,13−15] These hot carriers have unequal rates of dissipation on metallic surfaces.[16,17] As a result, hot carriers with "slower" transfer rates between a nanostructure and the surrounding medium accumulate on metallic surfaces generating an electrostatic potential.[18−21] A growing body of evidence suggests that the electrostatic potential can be altered by light intensity.[20−25]

The intensity of electrostatic potential can be quantified via direct measurements of the rectified electric field (REF).[26−29] Optical rectification is a second-order nonlinear process in which collective oscillations of conductive elections on the surface of nanostructures are rectified to a constant (DC) electric field.[25] Using 4-thiobenzonitrile (4-TBN) as a molecular reporter, our group determined the relationship between the intensities of light and REF on the surface of gold, gold–platinum, and gold–palladium nanoplates (AuNPs, Au@PtNPs, and Au@PdNPs).[25] We found that with an increase in the light intensity REF exponentially increases on AuNPs, while REF increase on Au@PtNPs and Au@PdNPs has a hyperbolic dependence on the light intensity.

Experimental evidence recently reported by our and other research groups suggests that the electrostatic potential may determine rates and yields of plasmon-driven reactions.[30−32] Specifically, Jain's group showed that reduction of carbon dioxide on gold nanoparticles yields a broad spectrum of hydrocarbons including methane, ethane, and ethylene as well as propane and propene.[31,33] Sungju and Jain discovered that relative yield of these reaction products could be altered by light intensity used to catalyze this reaction.[32] Our group used tip-enhanced Raman spectroscopy (TERS), a modern analytical technique that demonstrates single-molecule sensitivity and Angstrom spatial resolution,[34−37] to investigate a relationship between rates of plasmon-driven processes and light intensity.[30,38,39] In TERS, the metalized scanning probe is brought in the close proximity to the sample surface.[37,40] Next, the probe is illuminated by light, which generates high electric field (electrostatic potential) in the tip−sample junction.[41,42] As was discussed above, the electrostatic potential triggers plasmon-driven reactions in the molecular analytes present directly under the tip. Simultaneously, high local density of the

Received: June 18, 2022
Revised: September 14, 2022
Published: September 19, 2022

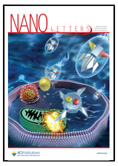

https://doi.org/10.1021/acs.nanolett.2c02428
Nano Lett. 2022, 22, 7484−7491

electric field enhances Raman scattering from the molecules present under the tip.[18,43] Thus, TERS allows to perform and simultaneously monitor plasmon-driven transformations at the nanoscale.[44−47] Using TERS, Li and co-workers found that an increase in the light intensity increases rates of 4-nitrobenzenethiol (4-NBT) to *p*,*p*′-dimercaptoazobisbenzene (DMAB) on both AuNPs and Au@PdNPs.[30] Specifically, we found that at 30 μW (λ = 633 nm) laser light rate constants of 4-NBT to DMAB reduction were k_{AuNPs} = 0.126 s^{-1} and $k_{\mathrm{Au@PdNPs}}$ = 0.071 s^{-1}, whereas at 150 μW the rates increased to k_{AuNPs} = 0.819 s^{-1} and $k_{\mathrm{Au@PdNPs}}$ = 0.477 s^{-1}. Our own results as well as experimental findings reported by other groups show that plasmon-driven reduction of 4-NBT on AuNPs yields only DMAB.[10,30,45,48] These studies provided a wealth of information about reaction mechanisms, kinetics, and thermodynamics of this reaction.[10,48−50] At the same time, the plasmon-driven reduction of 4-NBT on Au@PdNPs results in formation of both DMAB and 4-aminothiophenol (4-ATP).[43] These experimental findings suggest that the higher intensity of REF on Au@PdNPs than on AuNPs allows for reaching stronger reduction of 4-NBT on their surfaces.[18,25,30]

Expanding upon these findings, we hypothesize that light intensity can (i) change the yields of plasmon-driven reactions and (ii) alter the ratios of reaction products formed on bimetallic nanostructures. To answer these questions, we used TERS to determine the relationship between light intensity and the yield of plasmon-driven reductions of two molecular analytes: 3-mercaptobenzoic acid (3-MBA) and 4-NBT on AuNPs and Au@PdNPs.

REDOX TRANSFORMATIONS OF 3-MBA ON AuNPs and Au@PdNPs

The TERS spectrum of 3-MBA has three vibrational bands centered at 1074 and 1593 cm^{-1} that originate from the vibrations of the aromatic ring, as well as the band at 1714 cm^{-1}, which can be assigned to the COOH vibration (Figure 1). We found that on AuNPs 3-MBA decarbonylates forming thiophenol (TP) has four distinct vibrational bands at 997, 1025, 1076, and 1576 cm^{-1}.[51] Although the last two bands spatially overlap with the vibrational spectrum of 3-MBA, the presence of 997 and 1025 cm^{-1} in the collected TERS spectra can be used for unambiguous identification of TP on AuNP surfaces. Furthermore, on Au@PdNPs, we observed a reduction of 3-MBA to 3-mercaptophenylmethanol (3-MPM). This conclusion can be made by disappearance of 1714 cm^{-1} (COOH vibration) in some of the TERS spectra collected from Au@PdNPs (Figure 1). It should be noted that the disappearance of 1714 cm^{-1} cannot be due to change in molecular orientation relative to the metallic surface. Such changes in the molecular orientation would cause relative changes in the intensities of 1074 and 1593 cm^{-1} bands that were not observed in our studies.

TERS IMAGING OF PLASMON-DRIVEN TRANSFORMATION OF 3-MBA ON AuNPS and Au@PdNPs

An array of AuNPs and Au@PdNPs with a monolayer of 3-MBA was analyzed by TERS at different light intensities (60−1500 μW, λ = 633 nm) (Figure 2). Every pixel in the reported TERS maps has a full spectrum that reports the presence of certain molecular species on the surface of the nanostructures. In each experiment, we counted a number of pixels that indicate the presence of the products of catalytic reactions as well as the number of pixels that correspond to the reactant. Next, we determined the percentage of the pixels that correspond to the product of the catalytic transformation relative to the pixels that correspond to the reactant. Because all TERS maps were acquired with the same spatial resolution and the sizes of mono and bimetallic nanostructures used in

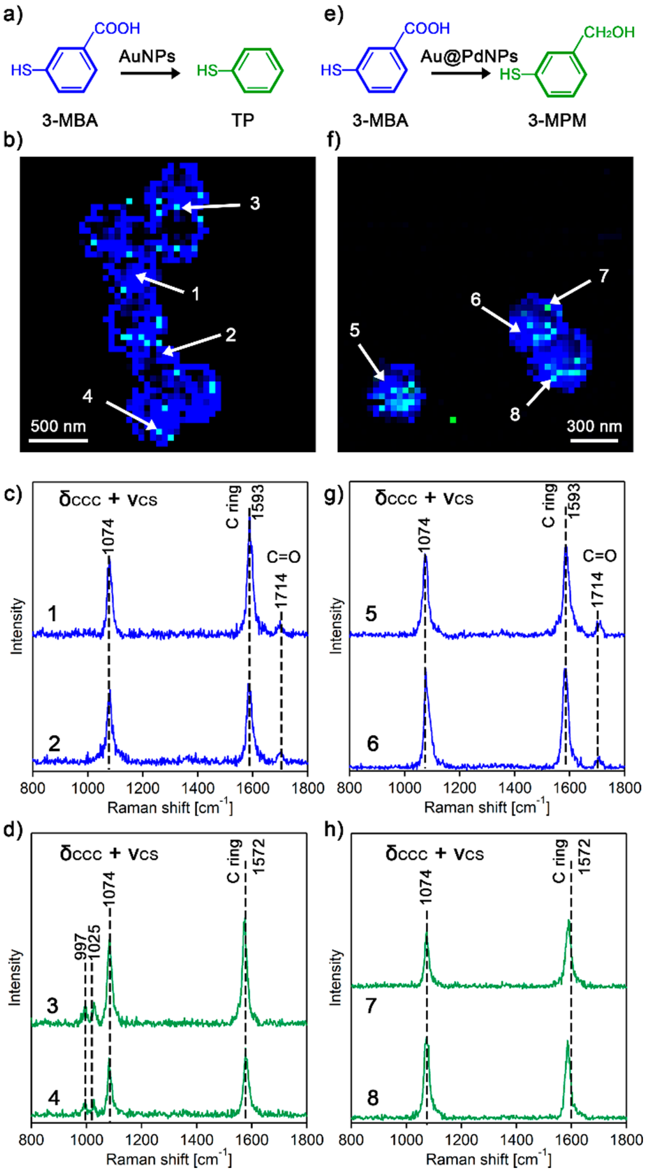

Figure 1. Plasmon-driven transformations of 3-MBA on AuNPs and Au@PdNPs. (a) A reaction scheme of 3-MBA decarboxylation to TP that is taken place on AuNPs and (b) a corresponding TERS image of AuNPs with 1714 cm^{-1} band (COOH vibration) of 3-MBA shown in blue and 997, 1025 cm^{-1} bands of TP shown in green. (c, d) Typical TERS spectra of 3-MBA (blue) and TP (green). The spectra are extracted from the TERS image of AuNPs (b). (e) Reaction scheme of 3-MBA reduction to 3-MPM that is taken place on Au@PdNPs. (f) The corresponding TERS image of Au@PdNPs with the 1714 cm^{-1} band (COOH vibration) of 3-MBA is shown in blue, and the spectra with a silent 1714 cm^{-1} band (3-MPM) are shown in green. (g, h) Typical TERS spectra of 3-MBA (blue) and 3-MPM (green) extracted from the TERS image of Au@PdNPs (f). The intensity ranges of 3-MBA and TP are both 10^4−10^5. The reported spectra are randomly picked from the TERS maps.

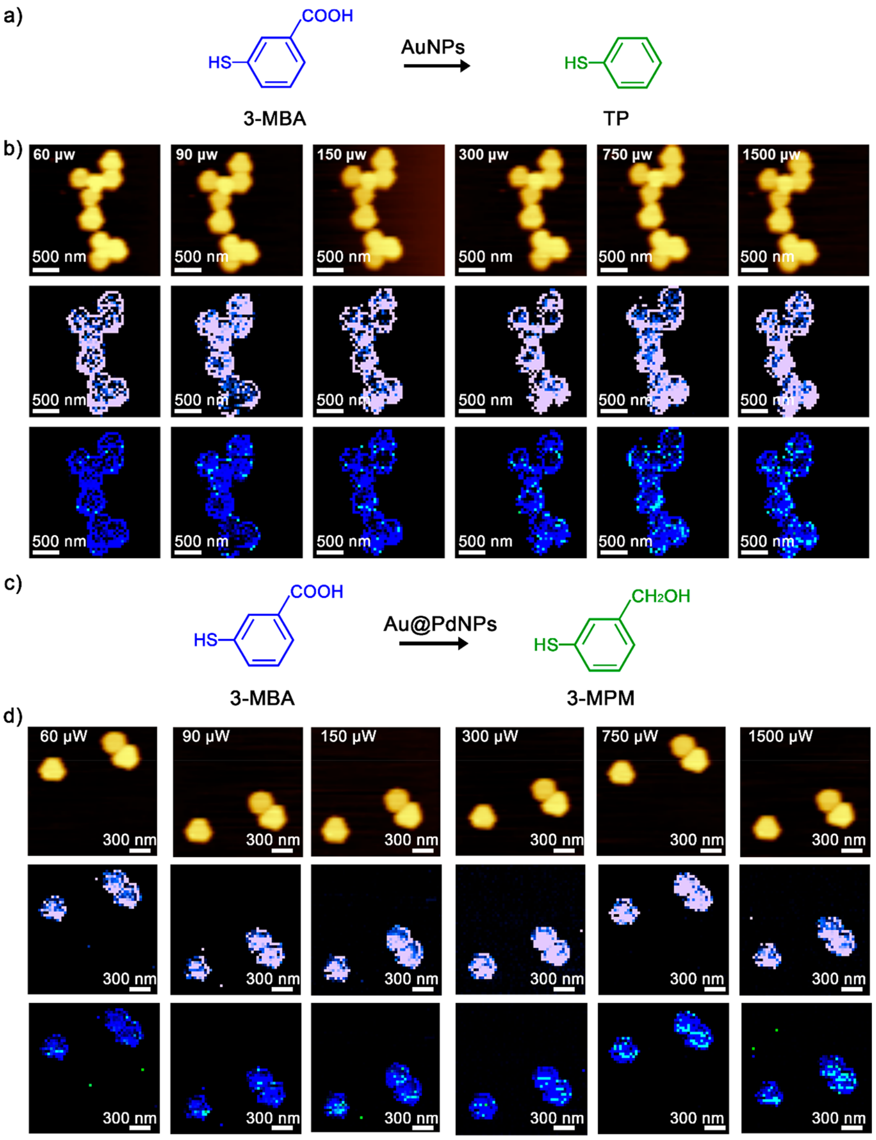

Figure 2. TERS imaging of 3-MPM reduction on AuNPs and Au@PdNPs formed at different light intensities (60−1500 μW) of 633 nm laser light. (a) Reaction scheme of 3-MBA to TP conversion on AuNPs. (b) In-situ AFM images (top row) of AuNPs and corresponding TERS images of COOH band (1714 cm^{-1}) of 3-MBA shown in blue (middle row) as well as the overlapped TERS images of COOH (blue) and C-ring vibrations (997, 1025 cm^{-1}) of TP (green) (bottom row). Scale bar is 500 nm in each map. (c) Reaction scheme of 3-MBA to 3-MPM conversion on Au@PdNPs. (d) In-situ AFM images (top row) of Au@PdNPs and corresponding TERS images of COOH band (1714 cm^{-1}) of 3-MBA shown in blue (middle row) as well as the overlapped TERS images of COOH (blue) and 3-MPM (absence of 1714 cm^{-1} band) (bottom row). Scale bar is 300 nm in each map. The intensity range of 3-MBATP and MPM is 104−105.

our studies very similar, this analytical approach allows for a TERS-based quantification of the yield of catalytic reactions

We found that with an increase in the light intensity the appearance of both TP on AuNPs and 3-MPM on Au@PdNPs increased. Specifically, at 60 μW, only 3.1% of all locations on AuNPs witnessed the presence of TP, whereas at 90 μW, the appearance of TP reached 5.4% (Figure 3 and Figure S1). We continued observing a graduate increase in the yield of TP from 8.7% at 150 μW to 23.5% at 1500 μW of the light intensity. A similar increase in the appearance of 3-MPM was observed on Au@PdNPs. At 60 μW, only 4.9% of all locations on Au@PdNPs revealed the presence of 3-MPM, whereas the appearance increased to 7.7% at 90 μW and continued increasing to 38.2% at 1500 μW (Figure 3 and Figure S1).

Direct comparison of the appearance of these reaction products at any of the discussed above light intensities shows that the yield of 3-MBA reduction to 3-MPM is always greater than the yield of 3-MBA decarboxylation to TP (Figure 3). We hypothesize that this difference in the reaction yields can be explained by the previously reported intensities of REF on Au@PdNPs and AuNPs exposed to the same light intensities.[25] This observation points on the direct relationship between light intensity, REF, and yields of plasmon-driven reactions.[18]

Our results also suggest that the reaction product itself is likely be determined by the catalytic metal (Pd) on bimetallic nanostructures. Pd demonstrates strong reduction properties that enables reduction of 3-MBA to 3-MPM on Au@PdNPs. The absence of Pd on AuNPs triggers a side-reaction of decarboxylation of 3-MBA to TP. One can expect that such decarboxylation reaction has different reaction mechanism. Yoon and co-workers proposed that holes from Au

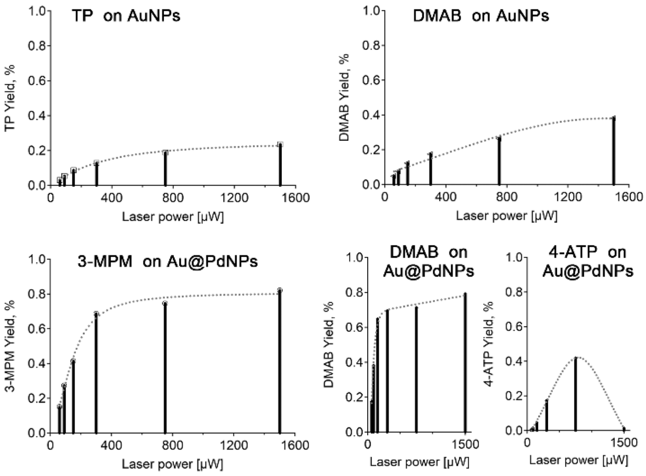

Figure 3. Intensity-dependent plots of TP on AuNPs (blue), DMAB on AuNPs (maroon), 3-MPM on Au@PdNPs (green), DMAB on Au@PdNPs (orange), and 4-ATP on Au@PdNPs (black) at different intensities (60−1500 μW) of 633 nm laser light.

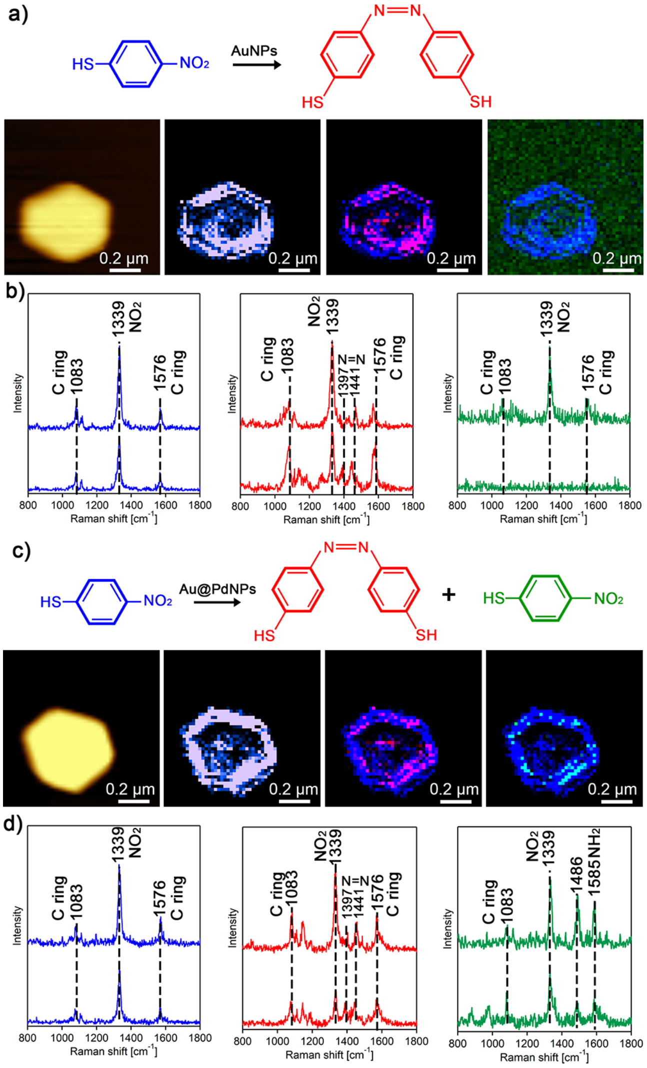

Figure 4. TER experiments of 4-NTP on AuNPs and Au@PdNPs. (a) TERS experiment of 4-NTP on AuNPs. The images from left to right are in-situ AFM, TERS map of 4-NTP, overlapping TERS image of 4-NTP and DMAB, and overlapping TERS image of 4-NTP and 4-ATP (no 4-ATP found), respectively (10 nm per pixel). The intensity of the 1339 cm^{-1} band (NO_2 vibration) of 4-NTP is shown in blue; the intensities of 1397, 1441 cm^{-1} (azo vibration) of DMAB are shown in red. (b) Typical TERS spectra extracted from chemical maps on AuNPs (a) showing the presence of 4-NTP (blue), DMAB (red), and without showing 4-ATP (green). (c, d) TERS experiment on Au@PdNPs showing the presence of 4-ATP; the intensity of 1485 cm^{-1} (NH_2 vibration) of 4-ATP is shown in green. The scale bar is 200 nm in each map. The intensity range of 4-NTP, 4-ATP, and DMAB is 10^4−10^5.

nanostructures transfer to the carboxyl group of 4-MBA, a similar molecular analyte, while corresponding hot electrons pass to protons.[52] This leads to a formation of carboxyl radicals and hydrogen atoms. The radicals then undergo intermolecular rearrangement causing C−C bond cleavage of 3-MBA. Thus, presence of Pd enables reduction of molecular species present on such bimetallic nanostructures, whereas the absence of this catalytic metal (palladium) directs plasmon-driven reactions toward C−C bond cleavage.

Nanoscale TERS imaging shows that both TP and 3-MPM are formed primarily at the edges of AuNPs and Au@PdNPs, respectively. Alternatively, these products could be simply more visible at the edges due to higher Raman scattering signal at the edges of AuNPs and Au@PdNPs. Utilization of an internal standard is required to disentangle these two possible explanation of the higher abundance of both TP and 3-MPM at the edges of AuNPs and Au@PdNPs, which is beyond the scope of the current work. It should be noted that, previously, we have demonstrated that both AuNPs and Au@PdNPs show higher intensities of REF at the edges of the nanostructures comparing to their flat terraces. This evidence further supports our hypothesis that yield of plasmon-driven reactions directly depends on REF intensities on mono- and bimetallic nanostructures.

■ PLASMON-DRIVEN REDUCTION OF 4-NBT ON AuNPs and Au@PdNPs

On AuNPs, the plasmon-driven reduction of 4-NBT results in formation of only DMAB, whereas both DMAB and 4-ATP could be observed as a result of 4-NBT reduction on Au@PdNPs. This conclusion can be made based on an appearance of the distinct vibrational fingerprints of DMAB (1083, 1339, 1397, 1441, and 1576 cm^{-1}) and 4-ATP (1083, 1339, 1486, and 1585 cm^{-1}) that are not evident for 4-NBT (1083, 1339, and 1576 cm^{-1}) (Figure 4).

We compared the amount of DMAB on AuNPs and DMAB vs 4-ATP at different light intensities (Figures 3 and 5). We observed nearly linear increase in the appearance of DMAB on AuNPs with an increase in the light intensity. Specifically, at 60 μW, only 15.1% of all locations on AuNPs witnessed formation of DAMB, whereas at 90 and 150 μW, the yield of DMAB was 27.4 and 41.5%. Finally, at 1500 μW, the appearance of DMAB was 82.1%. Similar to TP formation, we primarily observed appearance of DMAB around the perimeter of AuNPs.

We observed a similar relationship between the abundance of DMAB and the light intensity on AuNPs and Au@PdNPs. Within 60−300 μW, the appearance of DMAB on Au@PdNPs was found to be greater than the yield of DMAB on AuNPs (Figure 3). However, at 750 and 1500 μW, the appearance of DMAB on AuNPs was found to be slightly greater than the yield of DMAB on Au@PdNPs.

We also found that on Au@PdNPs the amount of 4-ATP can be altered by light intensity. At 30 μW, 4-ATP was present

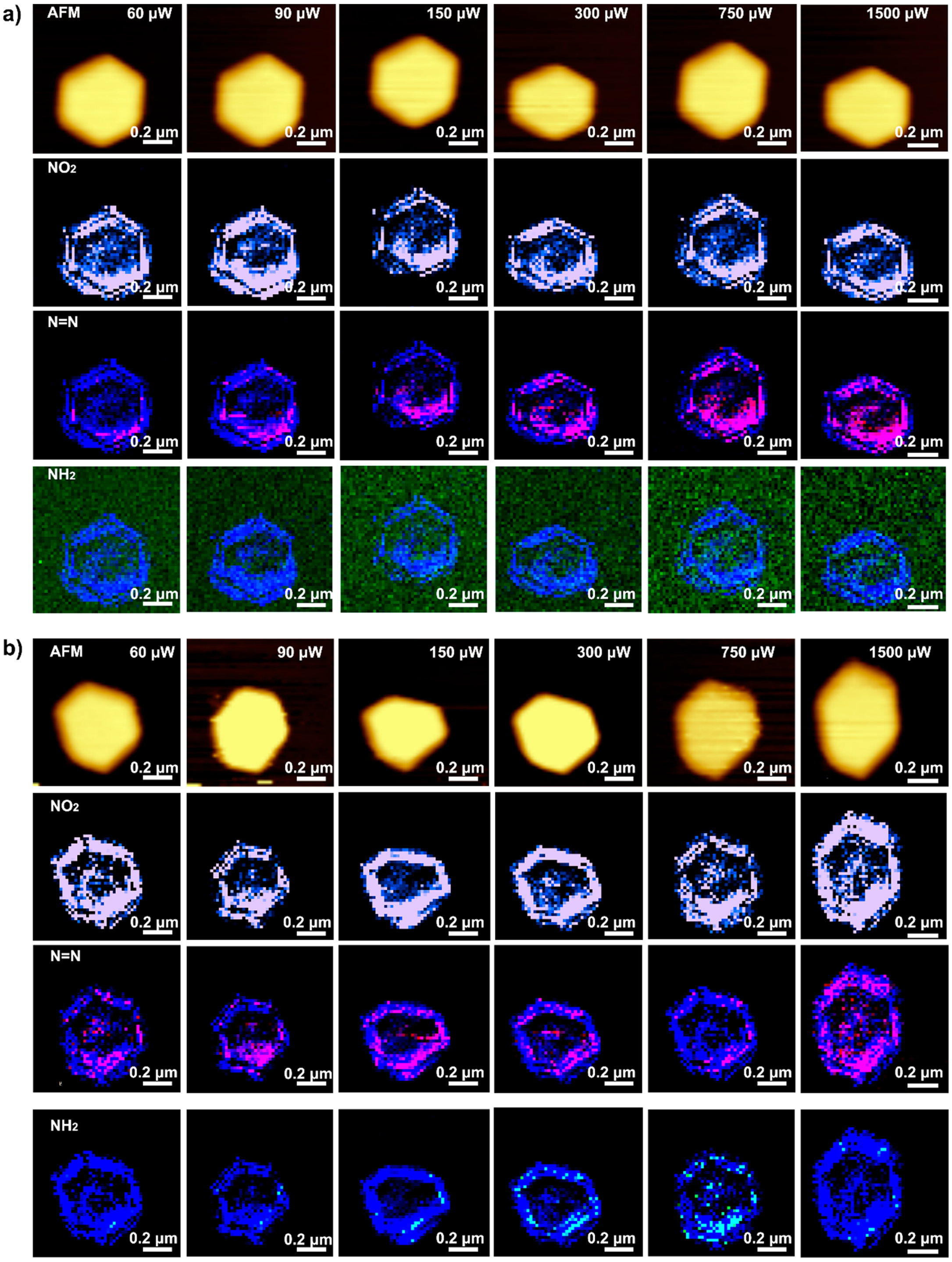

Figure 5. TERS imaging of (a) DMAB on AuNPs and (b) DMAB and 4-ATP on Au@PdNPs formed from 4-NBT at different light intensities (60−1500 μW) of 633 nm laser light. (a) In-situ AFM images (top row) of AuNPs and corresponding TERS images of 4-NBT (1339 cm^{-1}) shown in blue (middle row) as well as the overlapped TERS images of 4-NBT (blue) and DMAB (1397 and 1441 cm^{-1}) (red) (bottom row). (b) In-situ AFM images (top row) of Au@PdNPs and corresponding TERS images of 4-NBT (1339 cm^{-1}) shown in blue (middle row) as well as the overlapped TERS images of 4-NBT (blue), DMAB (1397 and 1441 cm^{-1}) (red), and 4-ATP (1486 cm^{-1}) (green) (bottom row). The scale bar is 200 nm in each map. The intensity range of 4-NTP, 4-ATP, and DMAB is 10^4−10^5.

on 0.5% of Au@PdNPs, whereas it gradually increased to 1.6% at 90 μW and 4.3% at 150 μW. Next, while the light intensity doubled, we observed more than 3 times increase in the abundance of 4-ATP at 300 μW. The maximum amount of 4-ATP was observed on Au@PdNPs at 750 μW (Figure 3). It should be noted that we primarily observed 4-ATP around the perimeter of Au@PdNPs. Interestingly, we observed a drastic decrease in the appearance of 4-ATP at 1500 μW. One can expect that at this laser intensity 4-ATP products can be further oxidizes to DMAB on Au@PdNPs, as suggested by Zhang and co-workers.[55] This behavior of yields of DMAB vs 4-ATP at different light intensities suggests that light intensity can be used to some extent to control the yield of DMAB vs 4-ATP. For instance, the use of 60 and 1500 μW will near exclusively yield DMAB. However, the tested gradient of light intensities will unlikely allow for production of high purity of 4-ATP on these bimetallic nanostructures. Nevertheless, we can conclude that light intensity can be used to alter yields of DMAB and 4-ATP on both AuNPs and Au@PdNPs.

It should be noted that we previously demonstrated that the same (4-ATP, 4-NBT, TP, and DMAB)[30] or similar molecular analytes (4-MBA) to the molecular reporters utilized in this work remain stable on the surface of the nanostructures upon their TERS imaging. These conclusions were made by continuous TERS imaging of the surface of mono- and bimetallic nanostructures with such analytes over the course of several hours, which proves absence of their photo or thermal degradation under used in this work experimental conditions. It is also important to emphasize that in our previous study we found that with an increase in the intensity of the laser light the intensity of the rectified electric field increased.[25] Our recent findings demonstrate that with an increase in the light intensity the yield of plasmon-driven reactions is increased. Thus, these two pieces of experimental evidence reveal the direct relationship between the light intensity and the yield of plasmon-driven reactions.

Our results show that the yield of plasmon-driven reduction of two molecular analytes, 3-MBA and 4-NBT, directly depends on the intensity of the laser light. We observed nearly linear relationship between the light intensity and the yield of TP on AuNPs that is formed by decarboxylation of 3-MBA. A similar relationship is observed for DAMB on AuNPs that is formed from 4-NBT. However, a logarithmic increase in the yield of 3-MBM on Au@PdNPs was observed with an increase in the laser intensity. Similar relationship between the yield of 4-ATP and the laser intensity has been observed for 4-NBT reduction on Au@PdNPs. It should be noted that a hyperbolic increase in the yield of DMAB was observed on these bimetallic nanostructures with increase in the intensity of the laser light. These findings point out on the different catalytic mechanisms of 3-MBA decarboxylation and reduction to 3-MBM as well as reduction of 4-NBT to DMAB and to 4-ATP.

Our findings also show that edges of both AuNPs and Au@PdNPs exhibit greater values of the electric field than flat terraces of both mono- and bimetallic nanostructures. This observation is in the good agreement with experimental and theoretical results reported by our own and Ren's groups,[25,53,54] which demonstrated higher densities of rectified electric field at these surface sites.

■ ASSOCIATED CONTENT

Supporting Information

The Supporting Information is available free of charge at https://pubs.acs.org/doi/10.1021/acs.nanolett.2c02428.

> Experimental details of the performed preparation of AuNPs, Au@PdNPs, scanning probes, as well as TERS measurements and assessment of the reaction yield; Figure S1: histograms of the yield of TP on AuNPs (blue), DMAB on AuNPs (maroon), 3-MPM on Au@PdNPs (green), DMAB on Au@PdNPs (orange), and 4-ATP on Au@PdNPs (black) at different intensities (60–1500 μW) of 633 nm laser light; Table S1: number of TERS spectra that correspond to the reaction product relative to the total number of pixels in TERS maps acquired at 60, 90, 150, 300, 750, and 1500 μW (PDF)

■ AUTHOR INFORMATION

Corresponding Author

Dmitry Kurouski − *Department of Biochemistry and Biophysics, Texas A&M University, College Station, Texas 77843, United States; The Institute for Quantum Science and Engineering, Texas A&M University, College Station, Texas 77843, United States;* orcid.org/0000-0002-6040-4213; Phone: 979-458-3778; Email: dkurouski@tamu.edu

Author

Zhandong Li − *Department of Biochemistry and Biophysics, Texas A&M University, College Station, Texas 77843, United States*

Complete contact information is available at: https://pubs.acs.org/10.1021/acs.nanolett.2c02428

Notes

The authors declare no competing financial interest.

■ ACKNOWLEDGMENTS

We are grateful to AgriLife Research of Texas A&M for the provided financial support. We also acknowledge Governor's University Research Initiative (GURI) grant program of Texas A&M University, GURI Grant Agreement No. 12-2016, M1700437.

■ REFERENCES

(1) Kleinman, S. L.; Frontiera, R. R.; Henry, A. I.; Dieringer, J. A.; Van Duyne, R. P. Creating, characterizing, and controlling chemistry with SERS hot spots. *Phys. Chem. Chem. Phys.* **2013**, *15* (1), 21–36.

(2) Brown, R. J.; Milton, M. J. T. Nanostructures and nanostructured substrates for surface-enhanced Raman scattering (SERS). *J. Raman. Spectr.* **2008**, *39*, 1313–1326.

(3) Moskovits, M. Surface roughness and the enhanced intensity of Raman scattering by molecules adsorbed on metals. *J. Chem. Phys.* **1978**, *69*, 4159–4161.

(4) Gersten, J.; Nitzan, A. Electromagnetic Theory of Enhanced Raman-Scattering by Molecules Adsorbed on Rough Surfaces. *J. Chem. Phys.* **1980**, *73*, 3023–3037.

(5) Kerker, M.; Wang, D. S.; Chew, H. Surface enhanced Raman scattering (SERS) by molecules adsorbed at spherical particles. *Appl. Opt.* **1980**, *19* (19), 3373–88.

(6) King, F. W.; Van Duyne, R. P.; Schatz, G. C. Theory of Raman scattering by molecules adsorbed on electrode surfaces. *J. Chem. Phys.* **1978**, *69* (10), 4472–4481.

(7) Brown, A. M.; Sundararaman, R.; Narang, P.; Goddard, W. A., III; Atwater, H. A. Nonradiative plasmon decay and hot carrier dynamics: effects of phonons, surfaces, and geometry. *ACS Nano* **2016**, *10* (1), 957–966.

(8) Hartland, G. V. Optical studies of dynamics in noble metal nanostructures. *Chem. Rev.* **2011**, *111* (6), 3858–3887.

(9) Ma, J.; Wang, Z.; Wang, L.-W. Interplay between plasmon and single-particle excitations in a metal nanocluster. *Nat. Commun.* **2015**, *6*, 10107.

(10) Cortés, E.; Xie, W.; Cambiasso, J.; Jermyn, A. S.; Sundararaman, R.; Narang, P.; Schlücker, S.; Maier, S. A. Plasmonic hot electron transport drives nano-localized chemistry. *Nat. Commun.* **2017**, *8*, 14880.

(11) Zhou, L.; Zhang, C.; McClain, M. J.; Manjavacas, A.; Krauter, C. M.; Tian, S.; Berg, F.; Everitt, H. O.; Carter, E. A.; Nordlander, P.; Halas, N. J. Aluminum nanocrystals as a plasmonic photocatalyst for hydrogen dissociation. *Nano Lett.* **2016**, *16* (2), 1478–1484.

(12) Mukherjee, S.; Zhou, L.; Goodman, A. M.; Large, N.; Ayala-Orozco, C.; Zhang, Y.; Nordlander, P.; Halas, N. J. Hot-electron-induced dissociation of H_2 on gold nanoparticles supported on SiO_2. *J. Am. Chem. Soc.* **2014**, *136* (1), 64–67.

(13) Brongersma, M. L.; Halas, N. J.; Nordlander, P. Plasmon-induced hot carrier science and technology. *Nat. Nanotechnol.* **2015**, *10* (1), 25−34.

(14) Lauchner, A.; Schlather, A. E.; Manjavacas, A.; Cui, Y.; McClain, M. J.; Stec, G. J.; Garcia de Abajo, F. J.; Nordlander, P.; Halas, N. J. Molecular Plasmonics. *Nano Lett.* **2015**, *15* (9), 6208−14.

(15) Narang, P.; Sundararaman, R.; Atwater, H. A. Plasmonic hot carrier dynamics in solid-state and chemical systems for energy conversion. *Nanophotonics* **2016**, *5* (1), 96−111.

(16) Yu, S.; Jain, P. K. The Chemical Potential of Plasmonic Excitations. *Angew. Chem., Int. Ed.* **2020**, *59*, 2085−2088.

(17) Yu, S.; Wilson, A. J.; Heo, J.; Jain, P. K. Plasmonic Control of Multi-Electron Transfer and C-C Coupling in Visible-Light-Driven CO_2 Reduction on Au Nanoparticles. *Nano Lett.* **2018**, *18*, 2189−2194.

(18) Li, Z.; Kurouski, D. Plasmon-Driven Chemistry on Mono- and Bimetallic Nanostructures. *Acc. Chem. Res.* **2021**, *54* (10), 2477−2487.

(19) Wilson, A. J.; Devasia, D.; Jain, P. K. Nanoscale optical imaging in chemistry. *Chem. Soc. Rev.* **2020**, *49*, 6087−6112.

(20) Kim, Y.; Smith, J. G.; Jain, P. K. Harvesting multiple electron-hole pairs generated through plasmonic excitation of Au nanoparticles. *Nat. Chem.* **2018**, *10* (7), 763−769.

(21) Kim, Y.; Dumett Torres, D.; Jain, P. K. Activation energies of plasmonic catalysts. *Nano Lett.* **2016**, *16* (5), 3399−3407.

(22) Nelson, D. A.; Schultz, Z. D. The impact of optically rectified fields on plasmonic electrocatalysis. *Farad. Discuss.* **2019**, *214* (0), 465−477.

(23) El-Khoury, P. Z.; Schultz, Z. D. From SERS to TERS and Beyond: Molecules as Probes of Nanoscopic Optical Fields. *J. Phys. Chem. C Nanomater. Interfaces* **2020**, *124* (50), 27267−27275.

(24) Wang, C. F.; O'Callahan, B. T.; Kurouski, D.; Krayev, A.; Schultz, Z. D.; El-Khoury, P. Z. Suppressing Molecular Charging, Nanochemistry, and Optical Rectification in the Tip-Enhanced Raman Geometry. *J. Phys. Chem. Lett.* **2020**, *11* (15), 5890−5895.

(25) Li, Z.; Rigor, J.; Large, N.; El-Khoury, P.; Kurouski, D. Underlying Mechanisms of Hot Carrier-Driven Reactivity on Bimetallic Nanostructures. *J. Phys. Chem. C* **2021**, *125*, 2492−2501.

(26) Sheldon, M. T.; Van de Groep, J.; Brown, A. M.; Polman, A.; Atwater, H. A. Plasmoelectric potentials in metal nanostructures. *Science* **2014**, *346* (6211), 828−831.

(27) Marr, J. M.; Schultz, Z. D. Imaging Electric Fields in SERS and TERS Using the Vibrational Stark Effect. *J. Phys. Chem. Lett.* **2013**, *4* (19), 3268.

(28) Nelson, D. A.; Schultz, Z. D. Influence of Optically Rectified Electric Fields on the Plasmonic Photocatalysis of 4-Nitrothiophenol and 4-Aminothiophenol to 4,4-Dimercaptoazobenzene. *J. Phys. Chem. C* **2018**, *122*, 8581−8588.

(29) Bhattarai, A.; Crampton, K. T.; Joly, A. G.; Kovarik, L.; Hess, W. P.; El-Khoury, P. Z. Imaging the Optical Fields of Functionalized Silver Nanowires through Molecular TERS. *J. Phys. Chem. Lett.* **2018**, *9* (24), 7105−7109.

(30) Li, Z.; Wang, R.; Kurouski, D. Nanoscale Photocatalytic Activity of Gold and Gold-Palladium Nanostructures Revealed by Tip-Enhanced Raman Spectroscopy. *J. Phys. Chem. Lett.* **2020**, *11* (14), 5531−5537.

(31) Devasia, D.; Das, A.; Mohan, V.; Jain, P. K. Control of Chemical Reaction Pathways by Light-Matter Coupling. *Annu. Rev. Phys. Chem.* **2021**, *72*, 423−443.

(32) Yu, S.; Jain, P. K. Plasmonic photosynthesis of C1-C3 hydrocarbons from carbon dioxide assisted by an ionic liquid. *Nat. Commun.* **2019**, *10* (1), 2022.

(33) Devasia, D.; Wilson, A. J.; Heo, J.; Mohan, V.; Jain, P. K. A rich catalog of C-C bonded species formed in CO_2 reduction on a plasmonic photocatalyst. *Nat. Commun.* **2021**, *12* (1), 2612.

(34) Cai, Z. F.; Zheng, L. Q.; Zhang, Y.; Zenobi, R. Molecular-Scale Chemical Imaging of the Orientation of an On-Surface Coordination Complex by Tip-Enhanced Raman Spectroscopy. *J. Am. Chem. Soc.* **2021**, *143* (31), 12380−12386.

(35) Lee, J.; Crampton, K. T.; Tallarida, N.; Apkarian, V. A. Visualizing vibrational normal modes of a single molecule with atomically confined light. *Nature* **2019**, *568* (7750), 78.

(36) Li, L.; Schultz, J. F.; Mahapatra, S.; Liu, X.; Shaw, C.; Zhang, X.; Hersam, M. C.; Jiang, N. Angstrom-Scale Spectroscopic Visualization of Interfacial Interactions in an Organic/Borophene Vertical Heterostructure. *J. Am. Chem. Soc.* **2021**, *143* (38), 15624−15634.

(37) Deckert-Gaudig, T.; Taguchi, A.; Kawata, S.; Deckert, V. Tip-enhanced Raman spectroscopy - from early developments to recent advances. *Chem. Soc. Rev.* **2017**, *46* (13), 4077−4110.

(38) Li, Z.; Kurouski, D. Probing the Redox Selectivity on Au@Pd and Au@Pt Bimetallic Nanoplates by Tip-Enhanced Raman Spectroscopy. *Acs Photonics* **2021**, *8* (7), 2112−2119.

(39) Li, Z.; El-Khoury, P.; Kurouski, D. Tip-Enhanced Raman Imaging of Photocatalytic Reactions on Thermally-Reshaped Gold and Gold-Palladium Microplates. *Chem. Commun.* **2021**, *57*, 891−894.

(40) Kurouski, D.; Dazzi, A.; Zenobi, R.; Centrone, A. Infrared and Raman chemical imaging and spectroscopy at the nanoscale. *Chem. Soc. Rev.* **2020**, *49* (11), 3315−3347.

(41) Kurouski, D.; Mattei, M.; Van Duyne, R. P. Probing Redox Reactions at the Nanoscale with Electrochemical Tip-Enhanced Raman Spectroscopy. *Nano Lett.* **2015**, *15* (12), 7956−62.

(42) Richard-Lacroix, M.; Zhang, Y.; Dong, Z.; Deckert, V. Mastering high resolution tip-enhanced Raman spectroscopy: towards a shift of perception. *Chem. Soc. Rev.* **2017**, *46* (13), 3922−3944.

(43) Yin, H.; Zheng, L.; Fang, W.; Lai, H. L.; Porenta, N.; Goubert, G.; Zhang, H.; Su, H. S.; Ren, B.; Richardson, J. O.; Li, J. F.; Zenobi, R. Nanometre- scale spectroscopic visualization of catalytic sites during a hydrogenation reaction on a Pd/Au bimetallic catalyst. *Nat. Catal.* **2020**, *3*, 834−842.

(44) Li, Z.; Kurouski, D. Probing the plasmon-driven Suzuki-Miyaura coupling reactions with cargo-TERS towards tailored catalysis. *Nanoscale* **2021**, *13* (27), 11793−11799.

(45) Li, Z.; Kurouski, D. Tip-Enhanced Raman Analysis of Plasmonic and Photocatalytic Properties of Copper Nanomaterials. *J. Phys. Chem. Lett.* **2021**, *12* (34), 8335−8340.

(46) Wang, C. F.; O'Callahan, B. T.; Kurouski, D.; Krayev, A.; El-Khoury, P. Z. The Prevalence of Anions at Plasmonic Nanojunctions: A Closer Look at p-Nitrothiophenol. *J. Phys. Chem. Lett.* **2020**, *11* (10), 3809−3814.

(47) Bhattarai, A.; El-Khoury, P. Z. Nanoscale Chemical Reaction Imaging at the Solid-Liquid Interface via TERS. *J. Phys. Chem. Lett.* **2019**, *10* (11), 2817−2822.

(48) Xie, W.; Schlucker, S. Surface-enhanced Raman spectroscopic detection of molecular chemo- and plasmo-catalysis on noble metal nanoparticles. *Chem. Commun.* **2018**, *54*, 2326−2336.

(49) van Schrojenstein Lantman, E. M.; Deckert-Gaudig, T.; Mank, A. J.; Deckert, V.; Weckhuysen, B. M. Catalytic processes monitored at the nanoscale with tip-enhanced Raman spectroscopy. *Nat. Nanotechnol.* **2012**, *7* (9), 583−586.

(50) Choi, H. K.; Park, W. H.; Park, C. G.; Shin, H. H.; Lee, K. S.; Kim, Z. H. Metal-Catalyzed Chemical Reaction of Single Molecules Directly Probed by Vibrational Spectroscopy. *J. Am. Chem. Soc.* **2016**, *138* (13), 4673−4684.

(51) Kurouski, D.; Large, N.; Chiang, N.; Greeneltch, N.; Carron, K. T.; Seideman, T.; Schatz, G. C.; Van Duyne, R. P. Unraveling near-field and far-field relationships for 3D SERS substrates-a combined experimental and theoretical analysis. *Analyst* **2016**, *141* (5), 1779−88.

(52) Huh, H.; Trinh, H. D.; Lee, D.; Yoon, S. How Does a Plasmon-Induced Hot Charge Carrier Break a C-C Bond? *ACS Appl. Mater. Interfaces* **2019**, *11* (27), 24715−24724.

(53) Zhong, J. H.; Jin, X.; Meng, L.; Wang, X.; Su, H. S.; Yang, Z. L.; Williams, C. T.; Ren, B. Probing the electronic and catalytic properties of a bimetallic surface with 3 nm resolution. *Nat. Nanotechnol.* **2017**, *12* (2), 132−136.

(54) Yin, H.; Zheng, L. Q.; Fang, W.; Lai, Y.-H.; Porenta, N.; Goubert, G.; Zhang, H.; Su, H. S.; Ren, B.; Richardson, J. O.; Li, J.-F.; Zenobi, R. Nanometre-scale spectroscopic visualization of catalytic sites during a hydrogenation reaction on a Pd/Au bimetallic catalyst. *Nat. Energy.* **2020**, *3*, 834−842.

(55) Zhang, J.; Winget, S. A.; Wu, Y.; Su, D.; Sun, X.; Xie, Z.-X.; Qin, D. Ag@Au Concave Cuboctahedra: A Unique Probe for Monitoring Au-Catalyzed Reduction and Oxidation Reactions by Surface-Enhanced Raman Spectroscopy. *ACS Nano* **2016**, *10*, 2607−2616.

https://doi.org/10.1021/acs.nanolett.2c02428
Nano Lett. 2022, 22, 7484−7491